

On the effect of the node and building orientation on the fatigue behavior of L-PBF Ti6Al4V lattice structure sub-unital elements

Simone Murchio^{1,2}  | Michele Dallago¹  | Andrea Rigatti¹ |
Valerio Luchin³ | Filippo. Berto⁴  | Devid Maniglio^{1,2}  | Matteo Benedetti¹ 

¹Department of Industrial Engineering – DII, University of Trento, Trento, Italy

²BIOtech Research Center, University of Trento, Trento, Italy

³Lincotek Additive, Pergine Valsugana, Trento, Italy

⁴Department of Mechanical and Industrial Engineering, NTNU – Norwegian University of Science and Technology, Trondheim, Norway

Correspondence

Simone Murchio, Department of Industrial Engineering – DII, University of Trento, Trento, Italy.
Email: simone.murchio@unitn.it

Abstract

Despite the great potential of additively manufactured (AM) metallic lattice materials, a comprehensive understanding of their mechanical behavior, particularly fatigue, has yet to be achieved. The role of the sub-unital lattice elements, that is, the struts and the nodes (or strut junctions), is rarely explored, even though it is well known that fatigue is a local phenomenon, determined by the small features of a structure (defects and local geometrical discontinuities).

In this work, the mechanical behavior of nodes and struts has been investigated by designing laser powder bed fusion (L-PBF) Ti6Al4V single strut specimens, with a node placed in the central part of the gauge length. The specimens were manufactured according to four different building orientations, namely, 90°, 45°, 15°, and 0° to the build plane. The influence of the fillet radius at the node and of the printing direction on the fatigue strength has been examined.

KEYWORDS

additive materials, fatigue, selective laser melting, Ta6v

1 | INTRODUCTION

The possibility of manufacturing lightweight, customizable, and complex-shaped components led to a rapid growth of metal additive manufacturing (AM) in the last few years. Until now, metal AM is considered a ground-breaking technology and finds its major applications in the biomedical, aerospace, and automotive fields.^{1,2} For instance, the introduction of architected cellular materials (also referred to as lattice structures) into the orthopedic field allowed to substantially reduce the stress shielding issue affecting traditional metal implants, simultaneously enhancing the osseointegration at the bone-implant interface, due to the tunable size and shape of the pores as well as the rough as-built surface.³

Nonetheless, despite the aforementioned major advantages, industries are still concerned about the application of architected cellular materials as components for structural integrity applications, such as load-bearing prosthetic

This is an open access article under the terms of the Creative Commons Attribution License, which permits use, distribution and reproduction in any medium, provided the original work is properly cited.

© 2021 The Authors. *Material Design & Processing Communications* published by John Wiley & Sons Ltd.

devices.⁴ In fact, metal AM techniques (i.e., powder bed fusion techniques such as L-PBF and electron beam powder bed fusion [EBPBF]) produce components with a high as-built surface texture, characterized by unmelted particles, protrusions, and material in excess on the external surfaces. These surface features can be detrimental to the mechanical properties of the printed items.⁵ Indeed, it is well known that the fatigue strength of a material is a local phenomenon, in which surface defects such as notches, imperfections, or local geometrical discontinuities might act as stress raisers, possibly leading to crack initiation and propagation, often till the specimen failure. A full understanding of the mechanical behavior of lattice structures is indeed of paramount importance for a better design and manufacturing of AM products. In this scenario, despite the static properties of lattice structures have been widely investigated in the literature, a consistent body of technical research on their fatigue behavior is still an open issue.⁶ Until now, most of the work has been addressed to the understanding of the fatigue response of different types of lattices but little work has been focused on the sub-unital elements of the cell units, namely, struts and junctions.^{7–9}

In a previous work of the authors,¹⁰ the fatigue behavior of thin struts and their dependency on the building orientation has been examined, while in the work of Dallago et al.¹¹ and of Latture et al.,¹² the role of strut junctions and of the fillet radius have been investigated in cubic and octet lattice structures, respectively. From these works, it has been revealed that junctions are a weak point of architected materials, due to the stress concentration and that improving the junction geometry by filleting can be beneficial in terms of fatigue resistance.¹¹

The aim of this work is to investigate the effect of the building orientation and the role of the fillet radius on the fatigue properties of the sub-unital elements of a cubic lattice cell. S–N fatigue curves have been obtained by performing an experimental campaign on L-PBF Ti6Al4V single strut specimens with a junction placed in the gauge length section. Specimens have been manufactured according to four different building orientations (90°, 45°, 15°, and 0°). Lastly, an investigation of the fracture surfaces of the four different batches has been carried out by SEM imaging.

2 | MATERIALS AND METHODS

2.1 | Specimen manufacturing and design

Round cross-section thin-strut specimens with a node placed in the middle section of the gauge length were designed as shown in Figure 1A, with a nominal diameter of 0.670 mm and a fillet radius of 0.600 mm. The transition zone between the gauge length (4 mm) and the grips was designed according to the “streamline fillet” rule, which theoretically has no stress concentration.¹³ Starting from a biomedical grade Ti6Al4V powder (particle size ranging from 15 to 45 μm), the strut-junction specimens were additively manufactured at Lincotek Medical (Trento, Italy) via L-PBF with an EOS M290 machine, with an actual laser power of 340 W and a scanning speed of 1250 mm/min. The layer thickness was set to 60 μm . A stripe scan pattern with 67° rotation from layer to layer was used for the inner bulk, plus a contour scan for the outer skin zone. The specimens were subsequently subjected to a proprietary heat treatment to remove residual stresses and to transform the α -martensitic as-built microstructure into a more stable $\alpha + \beta$ lamellar structure. No further surface treatments were performed on the specimens, which should be considered in an as-built condition.

These specimens were printed according to four different building orientations, namely, at 90°, 45°, 15°, and 0° with respect to the build plate (see Figure 1B).

2.2 | Morphological characterization

The morphological characterization of the four batches of specimens involved an analysis of the strut thickness, cross-sectional area, and fillet radius. The morphological characterization process was carried out initially collecting images of the specimens with a Nikon SMZ25 stereo optical microscope, as described in Murchio et al.¹⁰ Subsequently, an image analysis was performed using an in-house MATLAB routine (described in Murchio et al.¹⁰ and Dallago et al.¹⁴), first binarizing and segmenting the images and then extrapolating the desired data by fitting the boundaries. Strut thickness, cross-sectional area, and fillet radius at the node were calculated for each tested specimen. Finally, a minimum and an average value were obtained by averaging the sample data for each different building orientation.

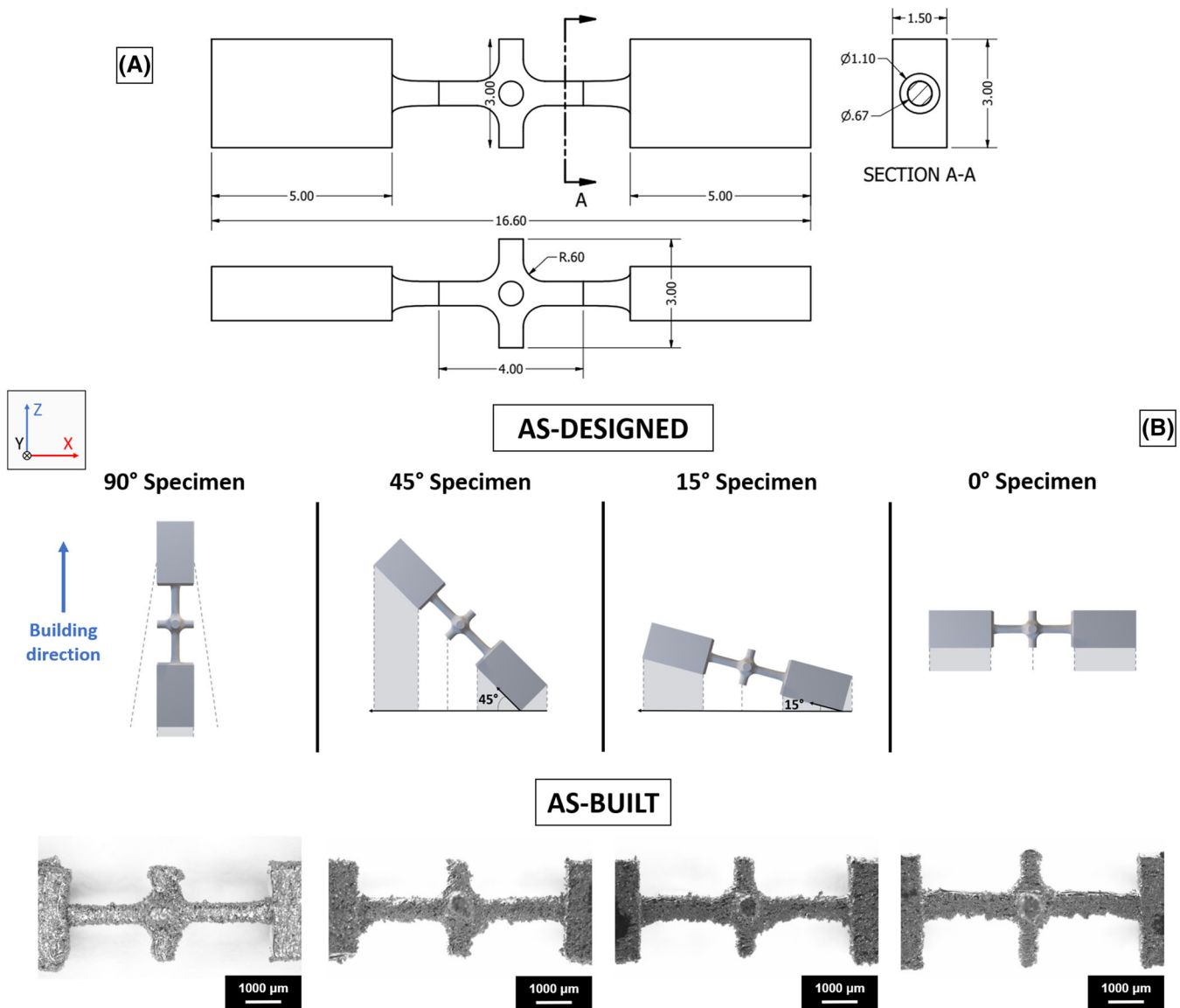


FIGURE 1 (A) Computer aided design (CAD) drawing of the strut specimen with junctions along the gauge length. Dimensions are reported in mm. (B) Schematic of the four sample building orientations, namely, at 90°, 45°, 15°, and 0° from the job plate. Supporting structures are indicated in light grey. The building direction is set as the Z axis of the reference system. For a visual comparison between the as-designed and as-built conditions, the stereo-optical images for each orientation are also reported. The scale bar is set to 1000 µm

2.3 | Fatigue testing

Load-controlled tension-compression fatigue tests ($R = -1$) with a constant amplitude sinusoidal wave form (nominal frequency of 200 Hz) were performed using a Bose Electroforce 3200, equipped with a 200-N load cell. Fatigue tests were conducted on the four specimen batches, until their failure or upon the runout threshold set at 10^7 cycles (labelled with an arrow). Runout samples were retested at loads 50% higher than the runout load. To build each S-N curve, at least 12 data points for each batch were collected, considering a minimum of four levels with three tested specimens for each level. Subsequently, a curve fitting was performed to plot the S-N curves and their scatter bands (10%–90%), as described in Murchio et al.¹⁰

2.4 | Surface fracture analysis

Field-emission scanning electron microscopy (FE-SEM, Zeiss Supra 40, Germany) was used to collect the fracture surface images of the fatigue failed specimens. SEM images were obtained in secondary electron mode with a 5.00-kV

acceleration. The fracture surfaces for each batch of specimens were investigated. All samples underwent surface cleaning by ultrasonication for 15 min, prior to the SEM inspection.

3 | RESULTS AND DISCUSSION

3.1 | Morphological characterization and fatigue tests

Table 1 reports the measured morphological parameters of the samples divided into the four different batches. The lowest minimum cross-sectional area is found in the 90° vertical struts, while the highest value is exhibited by the 0° strut-junction specimens. The standard deviation of the minimum and average cross-section and thickness is the highest in the 15° and 0° specimens. The standard deviation values can be considered as an indicator of the manufacturing precision of the specimens: therefore, the specimens printed at 90° and at 45° display lower variation of the cross-section size along the gauge length with respect to the specimens printed at lower angles to the build plane. Inclined specimens, for instance, are subjected to the “stair-case” effect and additionally the more inclined the specimen, the higher the downfacing surface texture is and the higher the presence of protrusions and material in excess can be.¹⁰

Figure 2 reports the S–N curves in a semi-logarithmic scale for the four different building orientations. The stress values have been calculated using three different cross-sectional areas, namely the nominal (Figure 2A), minimum (Figure 2B), and average cross-section (Figure 2C). For each graph, the thin-strut S–N curves (50% probability of failure) collected in Murchio et al.¹⁰ are also reported, to visually compare the fatigue behavior of struts with and without a node placed along the gauge length. Thin-strut specimens were printed using the same inclination angles, material, and process parameters as the specimens presented in this work. The fatigue limits of the four different batches are in the 30 and 80 MPa interval, falling in a comparable range with respect to the thin-strut specimens studied in Murchio et al.¹⁰ The evident discrepancies with respect to the wrought Ti6Al4V fatigue limits¹⁵ can be instead ascribed to the size-effect (high surface-to-volume ratio) and highly rough texture of the analyzed specimens.

In general, it is possible to state that the strut-junction specimens exhibit a lower fatigue life with respect to the thin-strut specimens, particularly in the case of the 90°, 45°, and 15° oriented batches. The decrease of fatigue strength of strut-junction specimens might be therefore ascribed to the presence of the node, acting as a weakening element of the component. Nevertheless, this trend is inverted for the 0° specimens, which report a higher fatigue strength with respect to the horizontally printed thin struts.

The effect of the building orientation on the S–N curves of the strut-junction specimens is less noticeable than in the case of the thin-strut specimens,¹⁰ particularly in the high cycle fatigue (HCF) regime, where the strut-junction S–N curves tend to overlap and are less scattered. This behavior can be probably ascribed to two main leading factors: the presence of the node in the central part of the gauge length (hence a shorter unsupported gauge length section) and the slightly larger average (and nominal) cross-section with respect to the previously studied thin-strut specimens (hence a lower surface-to-volume ratio), as reported in Table 1. The combination of these two factors might have led, in the case of the strut-junction specimens, to a lower surface defect sensitivity and a more regular cross-section variation along the gauge length, thus partially reducing the stress raising area where cracks can nucleate and propagate.

Conversely, in the low cycle fatigue (LCF) regime, the decrease of the fatigue life moving from the vertical 90° specimens to the horizontally printed 0° specimens is apparent, with a considerable drop of the fatigue resistance of the

TABLE 1 Cross-sectional areas, thicknesses, and fillet radii for the four differently oriented batches of specimens

	Cross-section (mm ²)			Thickness (μm)			Fillet radius (μm)		
	Nominal	Minimum	Average	Nominal	Minimum	Average	Nominal	Minimum	Average
90°	0.353	0.276 ± 0.014	0.321 ± 0.011	670	563 ± 26	639 ± 11	600	431 ± 76	772 ± 112
45°	0.353	0.326 ± 0.009	0.397 ± 0.007	670	595 ± 13	713 ± 7	600	431 ± 63	678 ± 51
15°	0.353	0.339 ± 0.031	0.426 ± 0.019	670	605 ± 22	739 ± 18	600	550 ± 90	737 ± 55
0°	0.353	0.342 ± 0.027	0.433 ± 0.022	670	605 ± 23	745 ± 19	600	492 ± 128	760 ± 102

Note: For all the parameters the nominal, minimum and average values, calculated among the tested specimens of the batches are reported. For average and minimum data, the standard deviations are also calculated.

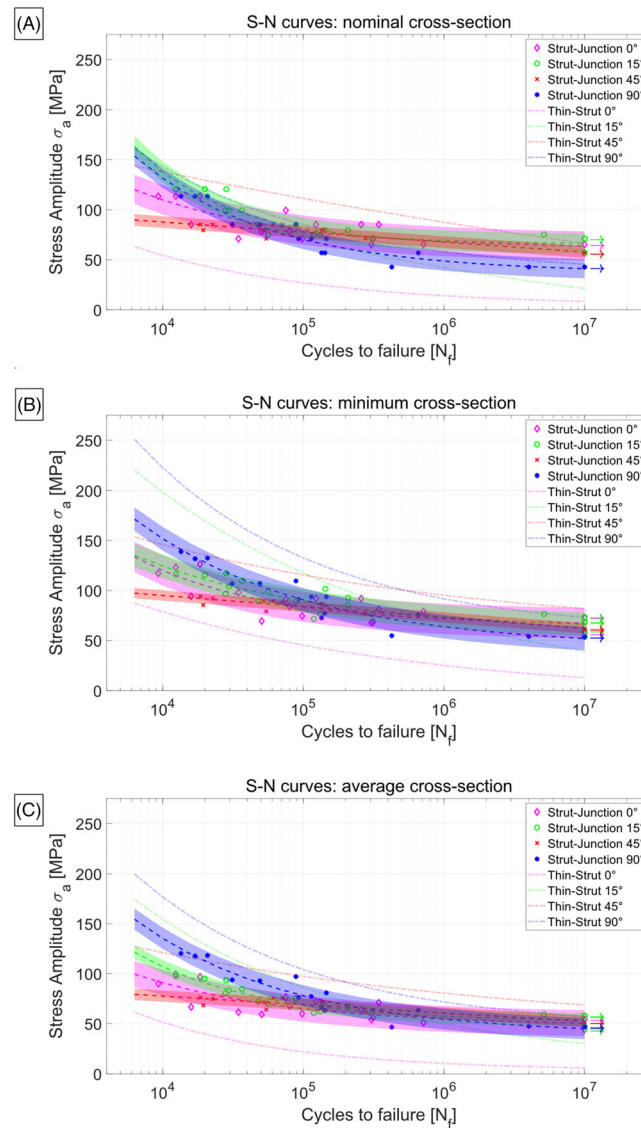


FIGURE 2 S–N semi-logarithmic curves of the fatigue strut-junction behavior according to the different building directions. Stress amplitude σ_A (MPa) is determined considering the nominal cross-section (A), minimum cross-section (B), and the average cross-section (C). Each S–N curve shows the experimentally collected data points and the fitting curve (dashed-line), representing the 50% probability of failure. For each S–N curve, the scatter bands referring to the 10–90% failure probability are also depicted. Runout is visually explicated by the presence of arrows (set at 10^7 cycles to failure, N_f). The dashed-dot S–N curves in each graph are the 50% probability of failure of thin struts specimens, experimentally derived in Murchio et al.,¹⁰ for the four building directions

specimens printed at 45° . This trend is again in accordance with the S–N curves reported in Murchio et al.,¹⁰ both considering the minimum or the average cross-section as load bearing areas.

A normalization of the S–N curves to the yield strength σ_y has been carried out (see Figure 3A,B; double logarithmic S–N curves) to better highlight the effect of defects and local geometrical variations, hiding the effect of the monotonic response of the material. The yield strength data were collected in Murchio et al.¹⁰ testing the thin-strut specimens. Reported yield strength values for the four different building directions are 770 MPa (for 90°), 562 MPa (for 45°), 952 MPa (for 15°), and 772 MPa (for 0°). Figure 3A,B reveals that 45° specimens exhibit the best fatigue life among the four batches, whereas 90° and 15° show the lowest fatigue strength in the HCF. Conversely, from Murchio et al.,¹⁰ where the horizontal thin-struts show the lowest fatigue behavior among the four investigated batches, the 0° strut-junction specimens have an intermediate behavior, lying between the 45° oriented and 90° oriented batches.

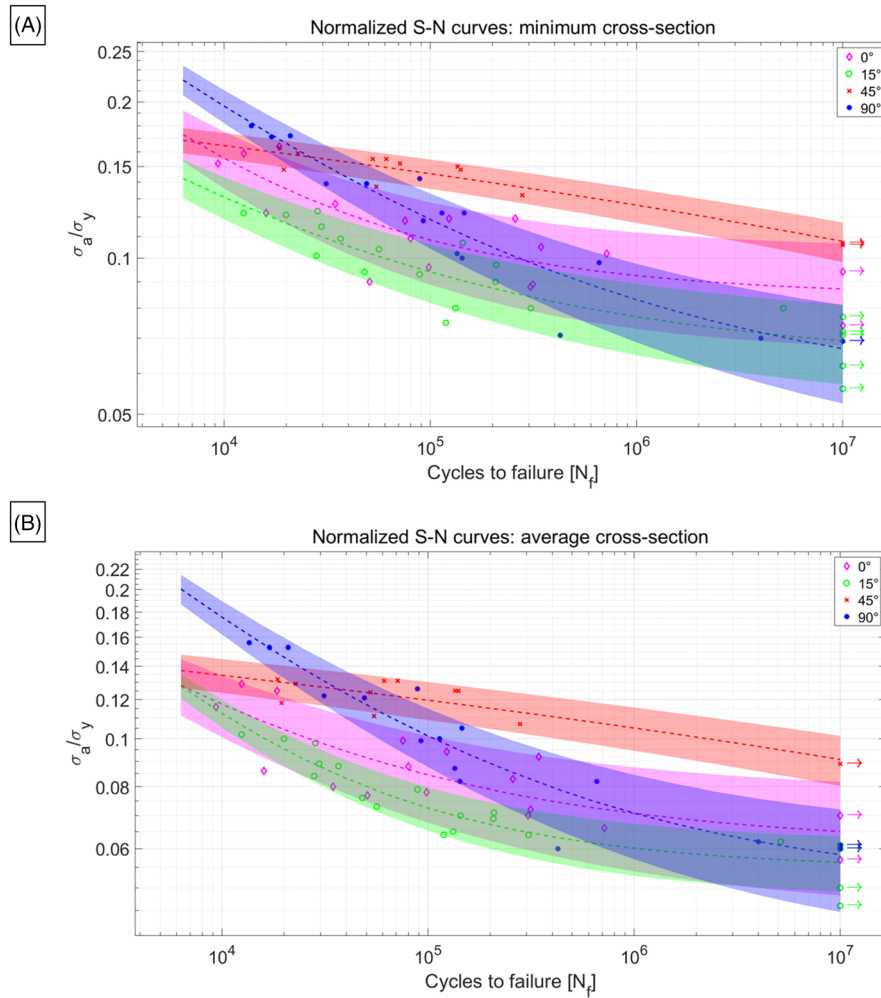


FIGURE 3 Yield strength normalized S–N curves are reported in a double logarithmic scale. In (A), the average cross-sectional area has been considered, while in (B), the average cross-section

3.2 | Surface fracture analysis

To understand the leading failure mechanisms of the struts with junctions, the fracture surface and the fracture location along the gauge length have been investigated. From this analysis, it has been revealed that the higher the printing accuracy along the gauge length is, the more prone the specimen is to break at the fillet radius or at the gripping site. Indeed, this is the case of 90° and 45° specimens, which show a lower standard deviation on the cross-section parameters with respect to the 15° and 0° struts, as highlighted in Table 1. It is well known that the surface texture and surface roughness of the specimens are strongly influenced by the building orientation,^{10,15–17} particularly with a lower surface roughness variation among the upperskin and underskin of the same specimen. This trend was studied in our previous work on thin-struts, as reported in Murchio et al.¹⁰ Since the strut-junction specimens were manufactured adopting the same printing parameters, scanning strategy, material, and geometrical dimensions, it is reasonable to believe that the surface roughness values should be in a comparable range with respect to thin-strut specimens (about 20–75 μm for the mean R_a value). The authors leave for future works a deeper metrological assessment of the strut-junction specimens. Additionally, it can be seen that the minimum fillet radius of the 90° and 45° specimens is consistently lower with respect to the 15° and 0° specimens (and with respect to the nominal fillet radius), thus suggesting that, for 90° and 45°, a higher stress concentration factor might arise at the node location. Conversely, for the 15° and 0° inclinations, the fracture location usually occurs at the gauge length. Moreover, as reported in the work on thin struts, 15° and 0° specimens exhibited the highest variation in terms of surface roughness between the upperskin and underskin of the same specimen (i.e., R_a range upper–lower skin of 75–145 μm).¹⁰ This might suggest that also in the

case of the 15° and 0° strut-junction specimens, the dominant fatigue failure mechanism can be imputed to the high surface defect sensitivity and local geometrical imperfections. In fact, these specimens exhibit a more evident cross-sectional size variation (see Table 1). This peculiar trend has also been observed in the work of Dallago et al.,¹¹ concerning cubic lattice structures, where it was noticed that if the main load bearing struts of the lattice were printed vertically (90°), fracture occurred at the node, alternatively, if the main load bearing struts were printed parallel to the build plane (0°), failure occurred along the strut gauge length. In Figure 4, the SEM fracture surfaces of one specimen for each batch are reported. SEM fracture images are coupled with a stereo-optical image labelling the fracture location site along the gauge length. Interestingly, the initial fracture location site is near the surface, where notches, cross-sectional variations and protrusions or unmelted particles act as stress raisers, causing the nucleation of several cracks. In most cases, it seems that the weaker site is located along the specimen lower skin, particularly for the 15° and 0° struts, where an evident cross-section thinning is present. In some cases, it also seems that cracks grow independently starting from multiple sites (i.e., 15° specimen) and that the subsequent crack propagation leads to failure on different cross-sectional planes. In Figure 4A (90° specimen), internal porosity, that is, gas holes or lack-of-fusion defects are also evident in proximity of the surface. These pores, if large enough, can act as “killer” defects, detrimentally influencing

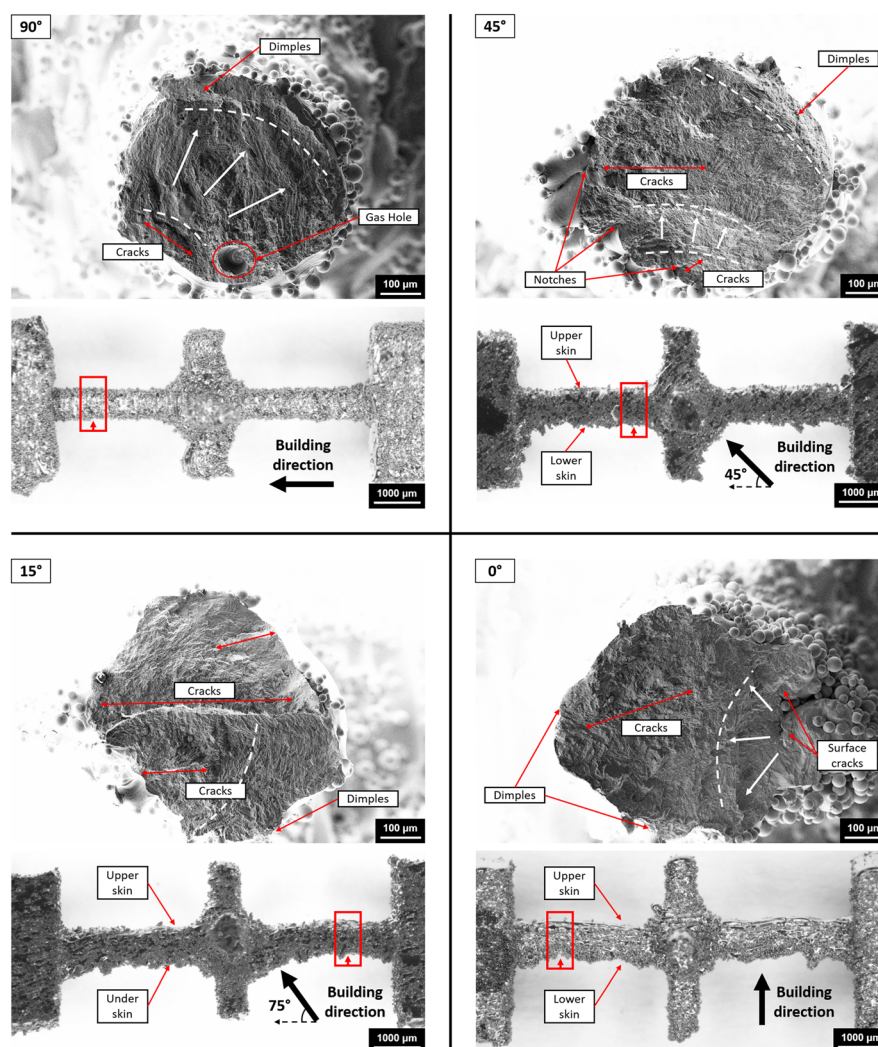


FIGURE 4 FE-SEM fracture surfaces of one fatigue failed specimen for each batch, as labelled. The scale bar is set to 100 μm for the four SEM images. White arrows and dotted curved lines show the initial crack nucleation and subsequent crack propagation, while red lines label instead the main cracks, notches, and defects detected on the fracture surfaces as well as the dimple locations. Each FE-SEM image is coupled with the stereo-optical image of the inspected specimen, highlighting the fracture location site along the gauge length (node or gauge length) with a red box. The upper and lower skin and the building direction are also labeled. The scale of the stereo-optical images is set to 1000 μm

the fatigue behavior of the strut-junction specimens. In this context, for the vertically printed struts, it might be reasonable to believe that a synergistic cooperation of the rough surface and the inner pores can be the cause of fatigue failure.

4 | CONCLUSIONS

In this work, the role of the sub-unital junction element on the fatigue life of L-PBF Ti6Al4V lattice elements has been addressed, with a particular focus on the effect of the building orientation. The experimental S–N fatigue curves show that vertically (90°) printed specimens have the highest fatigue strength in the LCF, while in the HCF, the strength is comparable between the four batches of specimens. Furthermore, the S–N curves normalized with respect to the yield strength of L-PBF Ti6Al4V at the different inclinations highlight the effect of building orientation even in the HC regime, with a slightly better response of the 45° strut-junction specimens, in accordance with what reported in Murchio et al.¹⁰ for thin-strut specimens. On the contrary, it appears that the fatigue life of the specimens printed horizontally is not affected as strongly as the thin-strut specimens by the orientation. This discrepancy might be related to the presence of the node along the gauge length, which limits the unsupported section of the gauge length during the manufacturing process, improving the morphological quality. Additionally, by the inspection of the fracture location, it is observed that the 90° and 45° strut-junction specimens are more prone to fail at the node location, due to the junction effect, than the 15° and 0° specimens. These specimens exhibit instead a failure mechanism more related to the high surface texture and cross-sectional variation, with the fracture location along the gauge length itself. Nevertheless, in both situations, the SEM fracture surfaces generally report surface defects as fatigue crack initiation sites.

DATA AVAILABILITY STATEMENT

The data that support the findings of this study are available from the corresponding author (Simone Murchio) upon reasonable request.

ORCID

Simone Murchio  <https://orcid.org/0000-0001-8058-834X>

Michele Dallago  <https://orcid.org/0000-0002-3836-7583>

Filippo. Berto  <https://orcid.org/0000-0001-9676-9970>

Devid Maniglio  <https://orcid.org/0000-0002-1653-861X>

Matteo Benedetti  <https://orcid.org/0000-0001-9158-2429>

REFERENCES

1. Horn TJ, Harrysson OLA. Overview of current additive manufacturing technologies and selected applications. *Sci Prog.* 2012;95(3): 255–282. <https://doi.org/10.3184/003685012X13420984463047>
2. Murr LE, Gaytan SM, Medina F, et al. Next-generation biomedical implants using additive manufacturing of complex, cellular and functional mesh arrays. *Philos Trans R Soc A Math Phys Eng Sci.* 2010;368(1917):1999–2032. <http://doi.org/10.1098/rsta.2010.0010>
3. Yadroitsava I, du Plessis A, Yadroitsev I. Bone regeneration on implants of titanium alloys produced by laser powder bed fusion: a review. *Titan Consum Appl.* 2019;197–233.
4. Zanetti EM, Aldieri A, Terzini M, Cali M, Franceschini G, Bignardi C. Additively manufactured custom load-bearing implantable devices: grounds for caution. *Australas Med J.* 2017;10(08):694–700. <https://doi.org/10.21767/AMJ.2017.3093>
5. Benedetti M, du Plessis A, Ritchie RO, Dallago M, Razavi SMJ, Berto F. Architected cellular materials: a review on their mechanical properties towards fatigue-tolerant design and fabrication. *Mater Sci Eng R Reports.* 2021;144(100606). <https://doi.org/10.1016/j.mser.2021.100606>
6. Zadpoor AA. Mechanical performance of additively manufactured meta-biomaterials. *Acta Biomater.* 2019;85:41–59. <https://doi.org/10.1016/j.actbio.2018.12.038>
7. Persenot T, Burr A, Martin G, Buffiere JY, Dendievel R, Maire E. Effect of build orientation on the fatigue properties of as-built electron beam melted Ti-6Al-4V alloy. *Int J Fatigue.* 2019;118:65–76. <https://doi.org/10.1016/j.ijfatigue.2018.08.006>
8. Suard M, Martin G, Lhuissier P, et al. Mechanical equivalent diameter of single struts for the stiffness prediction of lattice structures produced by electron beam melting. *Addit Manuf.* 2015;8:124–131. <https://doi.org/10.1016/j.addma.2015.10.002>
9. Pérez-Sánchez A, Yáñez A, Cuadrado A, Martel O, Nuño N. Fatigue behaviour and equivalent diameter of single Ti-6Al-4V struts fabricated by electron beam melting orientated to porous lattice structures. *Mater Des.* 2018;155:106–115.

10. Murchio S, Dallago M, Zanini F, et al. Additively manufactured Ti-6Al-4V thin struts via laser powder bed fusion: effect of building orientation on geometrical accuracy and mechanical properties. *J Mech Behav Biomed Mater*. 2021;119(104495). <https://doi.org/10.1016/j.jmbbm.2021.104495>
11. Dallago M, Raghavendra S, Luchin V, Zappini G, Pasini D, Benedetti M. The role of node fillet, unit-cell size and strut orientation on the fatigue strength of Ti-6Al-4V lattice materials additively manufactured via laser powder bed fusion. *Int J Fatigue*. 2021;142(105946). <https://doi.org/10.1016/j.ijfatigue.2020.105946>
12. Latture RM, Rodriguez RX, Holmes LR Jr, Zok FW. Effects of nodal fillets and external boundaries on compressive response of an octet truss. *Acta Mater*. 2018;149:78-87.
13. Pilkey WD, Pilkey DF. *Peterson's Stress Concentration Factors*. John Wiley & Sons; 2008.
14. Dallago M, Raghavendra S, Luchin V, Zappini G, Pasini D, Benedetti M. Geometric assessment of lattice materials built via selective laser melting. *Mater Today Proc*. 2019;7:353-361. <https://doi.org/10.1016/j.matpr.2018.11.096>
15. Pegues J, Roach M, Scott Williamson R, Shamsaei N. Surface roughness effects on the fatigue strength of additively manufactured Ti-6Al-4V. *Int J Fatigue*. 2018;116:543-552. <https://doi.org/10.1016/j.ijfatigue.2018.07.013>
16. Nakatani M, Masuo H, Tanaka Y, Murakami Y. Effect of surface roughness on fatigue strength of Ti-6Al-4V alloy manufactured by additive manufacturing. *Procedia Struct Integr*. 2019;19:294-301. <https://doi.org/10.1016/j.prostr.2019.12.032>
17. Klingaa CG, Dahmen T, Baier S, Mohanty S, Hattel J. Build orientation effects on the roughness of SLM channels. *Proc Jt Spec Interes Gr Meet between Euspen ASPE Adv Precis Addit Manuf*. 2019;111-114.

How to cite this article: Murchio S, Dallago M, Rigatti A, et al. On the effect of the node and building orientation on the fatigue behavior of L-PBF Ti6Al4V lattice structure sub-unital elements. *Mat Design Process Comm*. 2021;e258. <https://doi.org/10.1002/mdp2.258>